Illusion Optics via Phase-Gradient Metasurfaces

Zhaoyao Pan[1,2], Jinpeng Yang[1*], and Yadong Xu[2*]

[1]*College of Physical Science and Technology, Yangzhou University, Yangzhou 225009, China*
[2]*School of Physical Science and Technology & Jiangsu Key Laboratory of Frontier Material Physics and Devices, Soochow University, Suzhou 215006, China*

(Received 11 August 2025; accepted manuscript online 24 November 2025)

Optical phase-gradient metasurfaces have garnered significant attention for enabling flexible light manipulation, with applications across diverse domains. In this work, we will demonstrate that the metasurfaces with phase gradient modulation can be used to achieve illusion optics, featuring the advantages of simple geometric structure and feasible implementation compared with the well-known transformation optics method. The underlying mechanism is the anomalous diffraction law caused by the phase gradient, which provides a theoretical basis for freely manipulating the propagation path of light. By considering a specific example, we will demonstrate that the phase gradient can transform spatial coordinates in real space into illusion space, thereby converting a plane in real space into a curved surface structure in illusion space to achieve the illusion effect. This approach provides a viable alternative to transformation optics for designing illusion devices.

DOI: 10.1088/0256-307X/43/1/010401 CSTR: 32039.14.0256-307X.43.1.010401

1. Introduction. Metasurfaces emerge as versatile light-matter interfaces, leveraging their simplified structural design, subwavelength thickness and planar compactness to deliver unprecedented capabilities for wavefront manipulation.[1–4] In particular, phase-gradient metasurfaces (PGMs) have enabled a variety of transformative phenomena with considerable potential for practical applications, including anomalous wavefront control,[5–11] vortex beam generation,[12–19] metalenses,[20–22] and quantum communication.[23–25] In addition to single-layer configurations, the flexibility afforded by multi-layered structures has given rise to distinct phenomena, such as asymmetric transmission.[26–28] These advancements collectively underscore the extensive application potential of PGMs. Here, we will further show the use of multi-layered PGMs to achieve illusion optics.

Illusion optics[29,30] refers to a phenomenon whereby an object of arbitrary shape and material properties can be perceived as an entirely distinct object with a different geometry and material composition. The well-known method for achieving illusion optics is transformation optics (TO),[30] which is based on the invariance of Maxwell's equations under coordinate transformations. Moreover, TO can also be used to design devices to realize amusing phenomena such as cloaking,[31,32] invisible gateway[33] and optical black hole.[34] However, the material parameters of TO-based devices (including the illusion devices) are usually complex and extreme, posing great challenges to experiments.

In this work, we propose a PGM-based methodology for achieving illusion optics. This approach generates an optical effect analogous to a mirage by designing and exploring a system comprising a PGM and a perfect electric conductor (PEC) arranged in a parallel configuration. Due to the phase gradient, the reflection and refraction of light at the interface follow anomalous diffraction laws,[35] which can freely control the propagation direction of light. We will show that the phase gradient can transform the spatial coordinates in real space into illusion space, and specifically, a plane in real space can be transformed to a curved surface in illusion space to achieve the illusion effect. Previously, there were also some works that utilized metasurfaces to achieve cloaking,[36–38] in which the mechanism is based on phase gradient-enabled momentum compensation. These devices operate only at predetermined incident angles, limiting their angular adaptability. This proposal of PGM-based method enables effective realization of illusion optics over a wide angular range and offers a certain degree of design flexibility, as well as provides a promising pathway to address the limitations inherent in TO.

2. Models and Theory. As depicted in Fig. 1(a), the designed illusion optical system comprises a PGM and a PEC arranged in parallel. The PGM consists of periodically repeated supercells, each composed of m unit cells [see Fig. 1(b)]. In this configuration, m is selected as an even number to ensure that when the phase gradient equals k_0, the light wave undergoes anomalous transmission. The PEC can be a metallic material such as gold, ensuring that the light wave experiences specular reflection upon contacting the PEC and subsequently re-passes through the PGM. In this study, $m = 2$ is considered as an example. The initially designed frequency is $f_0 = 10\,\text{GHz}$, and the geometric parameters of the supercell are specified

*Corresponding authors. Email: yangjp@yzu.edu.cn; ydxu@suda.edu.cn
© 2026 Chinese Physical Society and IOP Publishing Ltd. All rights, including for text and data mining, AI training, and similar technologies, are reserved.

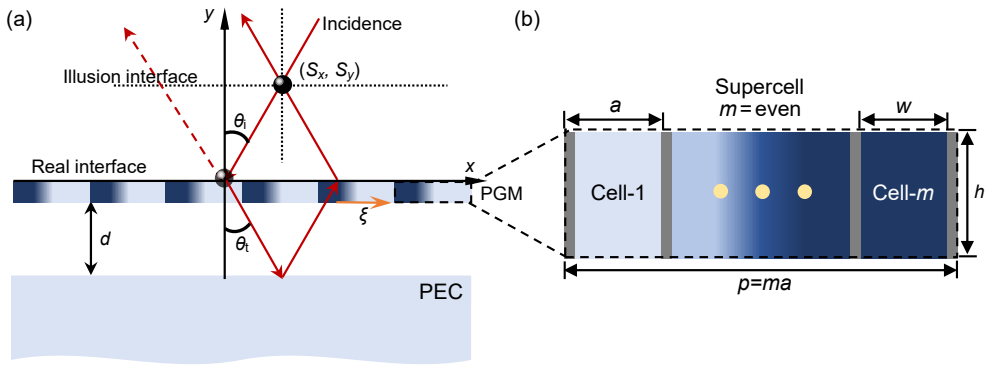

Fig. 1. Concept of illusion optics based on PGM. (a) Schematic diagrams and operational principle of illusion optics, where a PGM consisting of a supercell array is placed above a PEC substrate. (b) Geometry of the supercell composed of m unit cells, which is a subwavelength metallic slit array filled with different media.

as follows: $p = \lambda_0 = h = c/f_0$, $a = p/m$. The equivalent refractive index of each unit is determined according to $n_j = 1 + (j-1)\lambda_0/mh$ (h is the height of the PGM). The distance between the PGM and the PEC is denoted as d.

When a TM-polarized light (i.e., with the magnetic field oriented along the z-direction) is incident at an angle θ_i to the PGM and passes through it, an abrupt phase shift $\varphi(x) = n_j k_0 + \phi_0$ of complete 2π change is introduced at the interface, where ϕ_0 is a constant initial value, which induces a phase gradient of $\nabla\varphi(x) = k_0$ along the x-direction. Such phase gradient ensures an anomalous refraction in PGM, which is ruled by the following diffraction equation:[35,39]

$$\sin\theta_i = \sin\theta_t - n\frac{\xi}{k_0}, \tag{1}$$

where the integer n is the diffraction order, and θ_t is the refraction angle. For $\xi = k_0$, we have $\sin\theta_i = \sin\theta_t - n$. Based on Ref. [35], when $\theta_i < 0$, then $n = 1$; while $\theta_i > 0$, then $n = -1$, which indicates a negative refraction. After passing through the PGM, the transmitted wave subsequently undergoes specular reflection at the PEC interface and goes through the PGM again with negative refraction, eventually meeting the incident light at point S. Based on Eq. (1), the transmission angle of the secondary diffraction light is always equal to the angle of incidence, i.e., $\theta_t = \theta_i$, which means that a specular reflection occurs in the end. It should be emphasized that during this process, the diffraction efficiency is almost 100%.

In this optical process, for distant observers, the specular reflection that the eyes perceive occurs at point S with coordinates (S_x, S_y), rather than at the actual position S' corresponding to the origin (0, 0) of the coordinate system as indicated by the dashed line. This point is referred to as the illusion optical point or transformed coordinates, and the interface where this point resides is called the illusion interface. Such a phenomenon of reflection point deviation is similar to the Goos–Hänchen (GH) effect in wave optics, a fundamental phenomenon where the reflected wave experiences a lateral displacement or shift from the position predicted by geometric optics.[40,41] However, unlike the common GH effect, where the shift is determined by the medium itself, the PGM-enabled analogy can be freely controlled by both the phase gradient and separation d. The PGM-based methodology breaks through limitations of natural material properties and provides a unique approach to control and achieve desired GH displacement. Moreover, based on Eq. (1), coordinates (S_x, S_y) can be derived theoretically,

$$S_x = -d\Big[\tan\Big(\arcsin\frac{k_0\sin\theta_i - n\xi}{k_0}\Big)\Big], \tag{2}$$

$$S_y = d\Big|\tan\Big(\arcsin\frac{k_0\sin\theta_i - n\xi}{k_0}\Big)\Big/\tan\theta_i\Big|. \tag{3}$$

One can see that the transformed coordinates (S_x, S_y) are related to d, θ_i, and ξ. To validate the optical illusion, we will show the evolution of this illusion point with these parameters, employing both numerical simulations based on COMSOL Multiphysics and theoretical derivations.

3. Results and Discussions. To illustrate the above discussions, we take the case of $\xi = k_0$ as an example. The subsequent results shown in Fig. 4 will demonstrate that the case of $\xi = k_0$ can yield an expected illusion effect. We first investigate the relationship between transformed coordinates (S_x, S_y) and spacing d. For a fixed incident angle of $\theta_i = 30°$, figures 1(a) and 1(b) show the values of S_x and S_y for different d, respectively, i.e., $d = 0.5\lambda$, $d = 2\lambda$, $d = 3\lambda$, and $d = 4\lambda$. In these two plots, theoretical predictions based on Eqs. (2) and (3), along with simulation results, are very consistent; the transformed coordinates (S_x, S_y) exhibit a linear relationship with separation d. The rate of change in the y direction is greater than that in the x direction. This consistency still holds when d is less than one wavelength. Figures 2(c) and 2(d) display the corresponding field patterns which clearly illustrate and further confirm the theoretical predictions. Likewise, for opposite incidence, i.e., $\theta_i = -30°$, similar results can be obtained (but they are not shown here), with only difference being that the sign of S_x is reversed; i.e., $-S_x$.

Furthermore, the transformed coordinates have an angular dispersion for fixed d. Figures 3(a) and 3(b) show the relationship between the transformed coordinates (S_x, S_y) and different incident angles θ_i when $d = 3\lambda$. Due to the diffraction symmetry of PGM, the transformed coordinates (S_x, S_y) yield the same results for opposite incidences but with reversed sign in S_x. Here, for clarity,

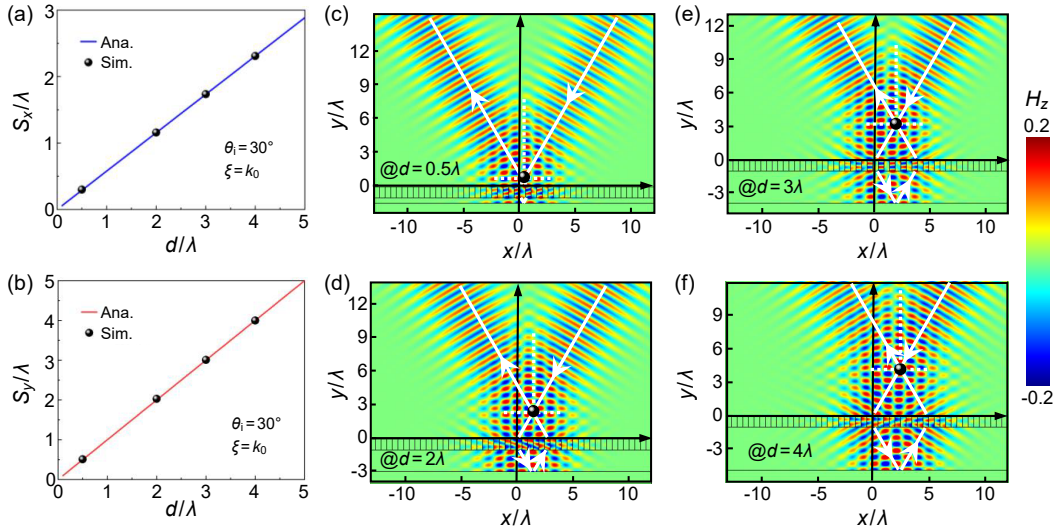

Fig. 2. Transformation coordinates (S_x, S_y) enabled by PGM with $\xi = k_0$ for different d. (a) and (b) The relationship between coordinates (S_x, S_y) and spacing d when $\theta_i = 30°$. (c)–(f) Magnetic field patterns for an incidence of a Gaussian beam with $\theta_i = 30°$, when $d = 0.5\lambda$, $d = 2\lambda$, $d = 3\lambda$, and $d = 4\lambda$.

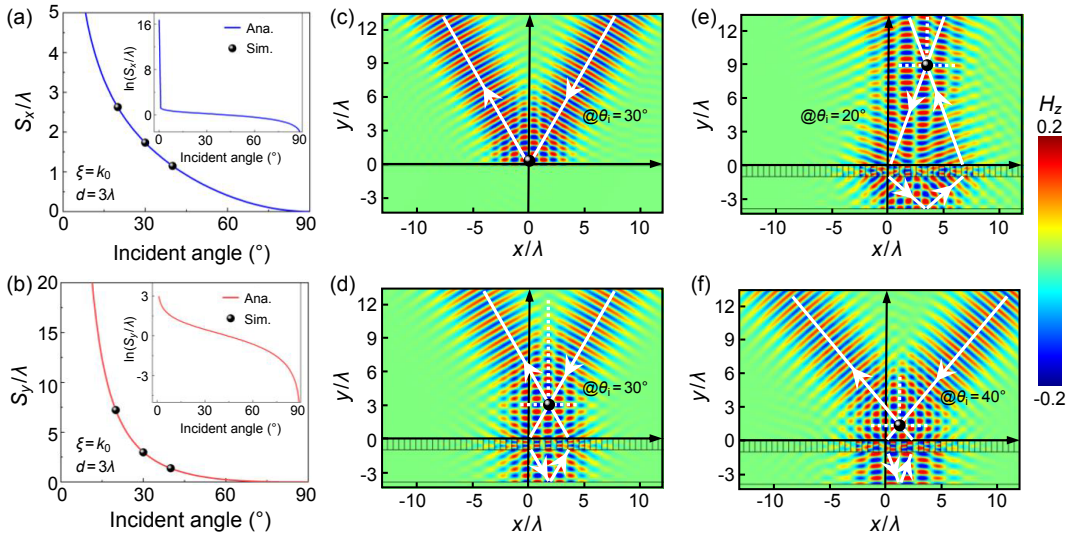

Fig. 3. Transformation coordinates (S_x, S_y) enabled by PGM with $\xi = k_0$ for different θ_i. (a) and (b) The (S_x, S_y) vs the incidence angle θ_i. (c) Magnetic field distribution when a Gaussian beam with $\theta_i = 30°$ is incident on the PEC at $y = 0$. (d)–(f) Magnetic field distribution when a Gaussian beam is incident on the PGM-based illusion system at incident angles of $\theta_i = 30°$, $\theta_i = 20°$, and $\theta_i = 40°$.

we only present the case of positive incidence. The results presented in Figs. 3(a) and 3(b) demonstrate that the theoretical predictions are in excellent agreement with the simulation results. As the incident angle increases from $\theta_i = 0°$ to $\theta_i = 90°$, the magnitudes of the two components of the transformed coordinates (S_x, S_y) exhibit a decreasing trend. Specifically, when the incident angle approaches zero, both components of the transformed coordinates increase significantly, as displayed by an enlarged plot. This is because $\theta_i = 0°$ corresponds to a diffraction transition point where diffraction is extremely intense, with its angle approaching 90°, thereby causing significant displacement. Of course, this normal incidence is just an ideal case which is extremely difficult to achieve in practice.

Figures 3(c) to 3(d) present the field patterns when a Gaussian beam with $\theta_i = 30°$ is incident on the air-PEC interface at $y = 0$ and the PGM-enabled system, respectively. We see that when our illusion optical system is positioned at the same level as the PEC, the illusion point within the illusion optical system exhibits a significant offset from the actual reflection point under far-field observation. For other incidences, such as $\theta_i = 20°$ or $\theta_i = 40°$, as shown by Figs. 3(e) and 3(f), the transformed coordinates increase correspondingly as the incident angle decreases. These results indicate that the optical illusion effect can be achieved across a broad range of incident angles.

Such an illusion effect caused by a PGM can be modulated by the phase gradient ξ, because it fundamentally determines the diffraction behavior of the PGM. Figures 4(a) and 4(b) illustrate parametric plots of (S_x, S_y) in two parameters: the phase gradient ξ and the incident angle θ_i when $d = 3\lambda$. The colored bar indicates the values of the transformed coordinates. Within the interval of $\xi/k_0 \in [0.5, 2]$, the diffraction of incident waves is governed

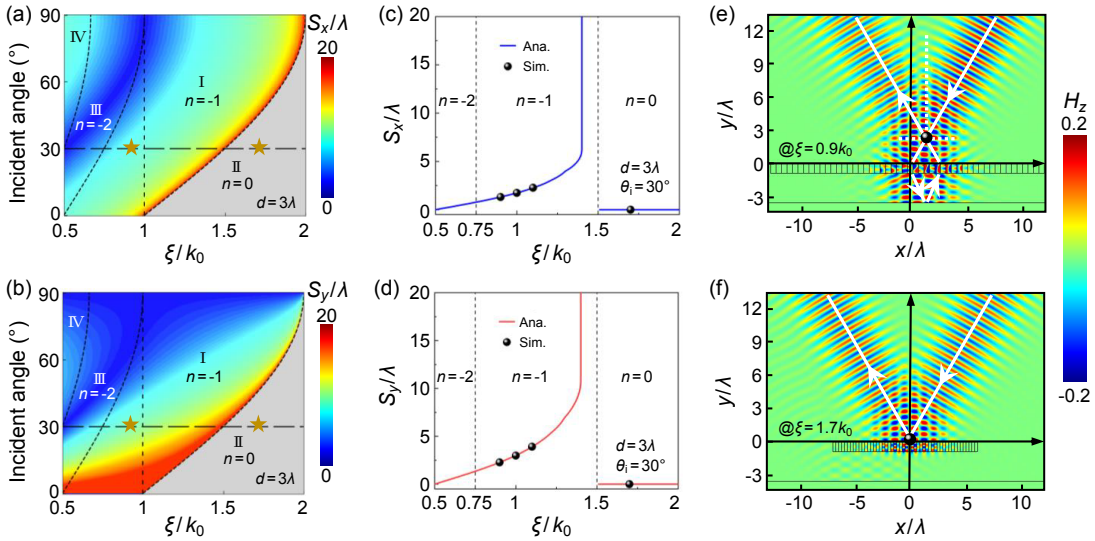

Fig. 4. Transformation coordinates (S_x, S_y) for different ξ. (a) and (b) The diagrams of (S_x, S_y) for the phase gradient ξ and the incident angle θ_i. (c) and (d) The relationship curves between the transformed coordinates (S_x, S_y) and the phase gradient ξ when $\theta_\mathrm{i} = 30°$. (e) and (f) The magnetic field patterns when $\xi = 0.9k_0$ and $1.7k_0$, where $\theta_\mathrm{i} = 30°$.

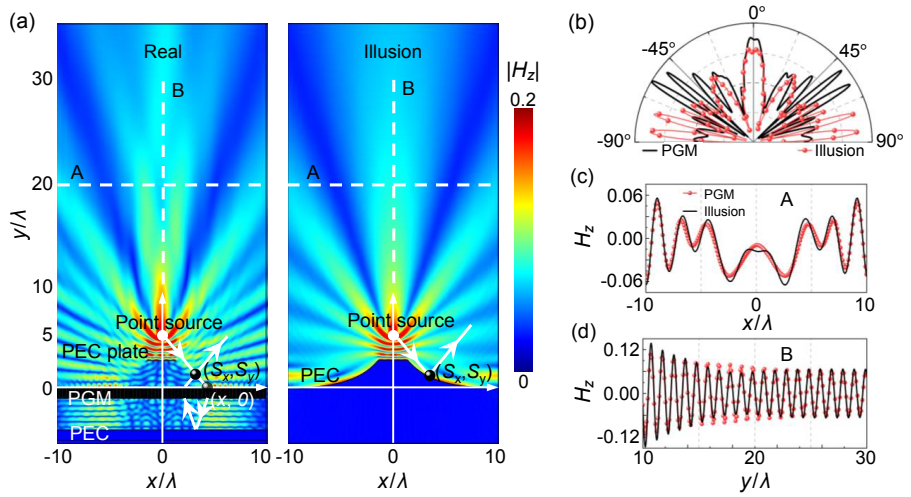

Fig. 5. Illusion device enabled by PGM. (a) Magnetic field pattern of a point source located in the PGM system, and the magnetic field pattern of the point source located in an equivalent illusion device, which is a curved PEC interface. (b) Two far-field patterns from (a). (c) and (d) are the line distributions of the magnetic field in the x direction and y direction in (a).

by four diffraction orders, i.e., $n = 0, -1, -2$, and -3. Based on these diffraction orders in the PGM, these diagrams can be segmented into four distinct regions as shown by black dotted curves. The gray area indicates the diffraction area of $n = 0$ order, which denotes a trivial region where no illusion occurs; i.e., $S_x = 0$ and $S_y = 0$. Specifically, Region I corresponds to coupling of the incident wave to order $n = -1$, where pronounced S_x and S_y are obtained. Figures 4(c) and 4(d) illustrate specific outcomes for system at $\theta_\mathrm{i} = 30°$ case. In this scenario, as the phase gradient increases, transformed coordinates also increase correspondingly and have a cutoff at $\xi = 1.5k_0$. Figures 4(e) and 4(f) display corresponding magnetic field distributions at $\xi = 0.9k_0$ and $\xi = 1.7k_0$ which confirm these findings.

The aforementioned results demonstrate that the illusion optics system can be manipulated by three degrees of freedom, which provides a way to mimic an illusion device. Here, we mainly utilize results from the diffraction Region I, where only one diffraction order appears, thereby ensuring a unique propagating path for the incident wave and very high/even perfect diffraction efficiency. Specifically, we examined an illusion optics system characterized by a phase gradient of $\xi = k_0$ and a spacing of $d = 3\lambda$, where the lengths of both the PGM and PEC are set to 10λ. Under these conditions, a point source, as depicted in Fig. 5(a), is positioned at $(0, 5\lambda)$ in real space. In this configuration, when light arrives at position $(x, 0)$ in real space, the incidence angle is given by $\tan\theta_\mathrm{i} = -x/(5\lambda)$. When it passes through the PGM system based on Eqs. (2) and (3), both S_x and S_y can be obtained, which correspond to the same coordinates (S_x, S_y) in illusion space [see Fig. 5(a)]. According to this coordinate (S_x, S_y), a curved boundary can be obtained as x changes from -10λ to 10λ,

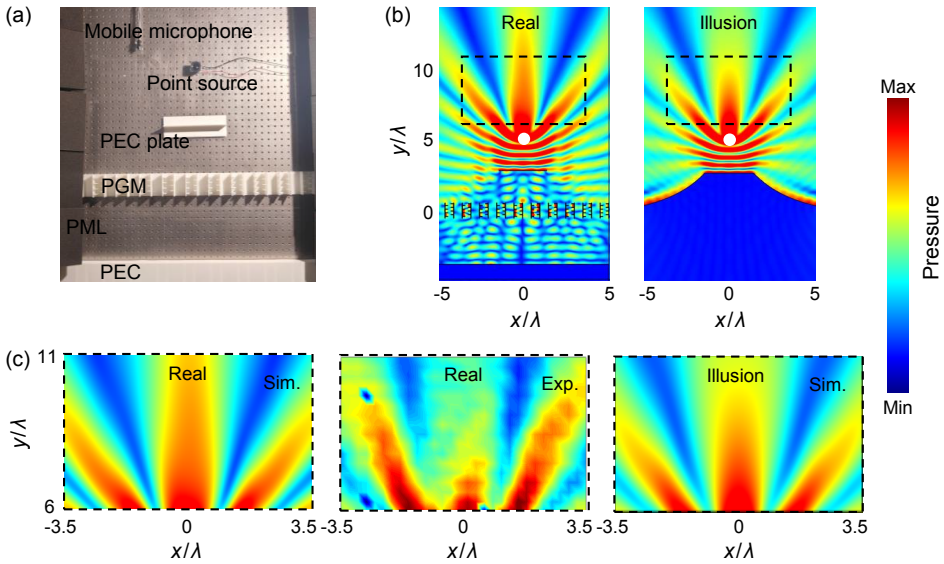

Fig. 6. Acoustic experimental demonstration of the illusion effect enabled by PGM. (a) Experimental setup. (b) Comparison of the simulated field patterns of the real system and the illusion system. (c) Comparison of experimental results with simulations in real and illusion spaces. The working frequency is 4000 Hz.

which is the PEC boundary considering the PEC substrate in real space. It should be noted that as x approaches 0, then $\tan\theta_{\rm i} = -x/(5\lambda)$; the transformed coordinates tend toward infinity, which presents significant implementation challenges. To address this issue, we implemented truncation in real space and introduced a PEC plate with a length of 2.9λ, positioned at a height of 3.1λ. It is necessary to emphasize that due to the limitations of the mechanism we proposed, the illusion effect demonstrated here is only applicable to the far field. Figure 5(b) presents the far-field radiation pattern of the optical system and its equivalent structure under specified detection conditions. Although these two results appear to differ to some extent, a more detailed examination reveals a high degree of consistency in their main lobe behavior. Additionally, figures 5(c) and 5(d) depict line distributions from Fig. 5(b) along the x and y directions, respectively. It can be observed that for magnetic field A at a height of 20λ and a length ranging from -10λ to 10λ on both the PGM and illusion optics system, the results are highly consistent in the x direction. In contrast, for magnetic field B with an x-axis value of 0 and a y-axis range from 10λ to 20λ in both cases, the magnitude and spatial distribution of the magnetic field are almost identical. Therefore, the equivalent results of the optical illusion system were obtained, which can be considered as actual observational outcomes perceived by observers, illustrating the effect of illusion optics.

The illusion device enabled by PGM was experimentally confirmed by acoustic waves. Figure 6(a) shows the schematic diagram of the experimental setup. The whole system is located in an air medium with a sound speed of 343 m/s, and the working frequency is 4000 Hz. The PGM structure illustrated in Fig. 5 can be implemented using acoustic configurations, which can be designed using a zigzag structure and fabricated via 3D printing technology. The PEC plate can be replaced by sound-hard materials, such as photosensitive resin.[35] Figure 6(b) presents the simulation results of the field pattern in both real space and illusion space corresponding to the experimental system. Figure 6(c) displays the field pattern obtained from the experiment in the rectangular region shown in Fig. 6(b), and it is in excellent agreement with the simulated ones.

4. Conclusion. In summary, we have proposed a method for realizing illusion optics based on a single-layer structure composed of PGM and PEC, which utilizes parity-reversed diffraction rules. Theoretical analysis and simulation results demonstrate that the proposed structure enables multi-degree-of-freedom control of the visual reflection point across a wide range of distances, incident angles, and phase gradients. Furthermore, the illusion effect of the structure was simulated from the observer's perspective, and the outcomes exhibit strong consistency with theoretical predictions, demonstrating a notable degree of flexibility. This approach offers a novel and practical solution for overcoming the limitations inherent in conventional TO within the domain of illusion optics.

Data Availability. The data supporting the findings of this study are available from the corresponding author upon reasonable request.

Acknowledgements. This work was supported by the National Natural Science Foundation of China (Grant Nos. 12274313 and 62375234), and the Gusu Leading Talent Plan for Scientific and Technological Innovation and Entrepreneurship (Grant No. ZXL2024400).

References

[1] Kildishev A V, Boltasseva A, and Shalaev V M 2013 *Science* **339** 1232009
[2] Sun S, He Q, Hao J, Xiao S, and Zhou L 2019 *Adv. Opt. Photonics* **11** 380
[3] Xu Y, Fu Y, and Chen H 2016 *Nat. Rev. Mater.* **1** 16067
[4] Guo J, Fang Y, Qu R, and Zhang X 2023 *Mater. Today* **66** 321

[5] Quan J, Xu L, Fu Y, Gao L, Chen H, and Xu Y 2024 *J. Acoust. Soc. Am.* **156** 2982
[6] Zhang L, Ding J, Zheng H, An S, Lin H, Zheng B, Du Q, Yin G, Michon J, Zhang Y, Fang Z, Shalaginov M Y, Deng L, Gu T, Zhang H, and Hu J 2018 *Nat. Commun.* **9** 1481
[7] Chen S, Fan Y, Yang F, Sun K, Fu Q, Zheng J, and Zhang F 2021 *Front. Mater.* **8** 790987
[8] Fang X, Li S, Sun B, Yan D, Yang J, Luo J, Gao D, and Xu Y 2025 *Chin. Phys. Lett.* **42** 034301
[9] Chen Y, Quan J, Gao Y, Sun B, Gao F, Fu Y, and Xu Y 2025 *Appl. Phys. Lett.* **126** 201704
[10] Lor C 2024 *Microsyst. Nanoeng.* **10** 40
[11] Gu S, Wang C, Gao Z, Gao L, Gao F, Wang S, and Xu Y 2025 *Chin. Phys. Lett.* **42** 090401
[12] Ren H, Briere G, Fang X, Ni P, Sawant R, Héron S, Chenot S, Vézian S, Damilano B, Brändli V, Maier S A, and Genevet P 2019 *Nat. Commun.* **10** 2986
[13] Ahmed H, Kim H, Zhang Y, Intaravanne Y, Jang J, Rho J, Chen S, and Chen X 2022 *Nanophotonics* **11** 941
[14] Chen Q, Qu G, Yin J, Wang Y, Ji Z, Yang W, Wang Y, Yin Z, Song Q, Kivshar Y, and Xiao S 2024 *Nat. Nanotechnol.* **19** 1000
[15] Hao Z, Chen H, Yin Y, Zhu S, Xu Y, Qiu C W, and Chen H 2024 *Sci. China Phys. Mech. Astron.* **67** 264311
[16] Wang Q, Zhou Z, Liu D, Ding H, Gu M, and Li Y 2022 *Sci. Adv.* **8** eabq4451
[17] Li R, Liu C, Wang L, Ma C, Wu J H, and Ma F 2024 *Commun. Phys.* **7** 188
[18] Zhang C, Jiang X, and Ta D 2024 *Phys. Rev. Lett.* **132** 114001
[19] Cao Y, Quan J, Sun B, Fang X, Hang Z, Gao L, Fu Y, and Xu Y 2024 *Appl. Phys. Lett.* **124** 132201
[20] Chen W T, Zhu A Y, Sanjeev V, Khorasaninejad M, Shi Z, Lee E, and Capasso F 2018 *Nat. Nanotechnol.* **13** 220
[21] Lee D, Oh B, Park J, Moon S W, Shin K, Kim S M, and Rho J 2024 *Nat. Commun.* **15** 3044
[22] Chang S, Zhang L, Duan Y, Rahman M T, Islam A, and Ni X 2024 *Nat. Commun.* **15** 9627
[23] Wang K, Titchener J G, Kruk S S, Xu L, Chung H P, Parry M, Kravchenko I I, Chen Y-H, Solntsev A S, Kivshar Y S, Neshev D N, and Sukhorukov A A 2018 *Science* **361** 1104
[24] Bekenstein R, Pikovski I, Pichler H, Shahmoon E, Yelin S F, and Lukin M D 2020 *Nat. Phys.* **16** 676
[25] Solntsev A S, Agarwal G S, and Kivshar Y S 2021 *Nat. Photonics* **15** 327
[26] Quan J, Sun B, Fu Y, Gao L, and Xu Y 2024 *Chin. Phys. Lett.* **41** 014301
[27] Zou H, Qian J, Xia J, Gu S, Lu Y, Ge Y, Yuan S, Chen H, Sun H, Yang Y, and Zhang B 2024 *J. Acoust. Soc. Am.* **156** 1920
[28] Zou H, Ge Y, Zhao K, Lu Y, Si Q, Yuan S, Chen H, Sun H, Yang Y, and Zhang B 2024 *Adv. Mater.* **36** 2401738
[29] Lai Y, Ng J, Chen H, Han D, Xiao J, Zhang Z Q, and Chan C T 2009 *Phys. Rev. Lett.* **102** 253902
[30] Xu Y, Du S, Gao L, and Chen H 2011 *New J. Phys.* **13** 023010
[31] Leonhardt U 2006 *Science* **312** 1777
[32] Chen H, Chan C T, and Sheng P 2010 *Nat. Mater.* **9** 387
[33] Ye K P, Pei W J, Sa Z H, Chen H, and Wu R X 2021 *Phys. Rev. Lett.* **126** 227403
[34] Ba Q, Zhou Y, Li J, Xiao W, Ye L, Liu Y, Chen J, and Chen H 2022 *eLight* **2** 19
[35] Fu Y, Shen C, Cao Y, Gao L, Chen H, Chan C T, Cummer S A, and Xu Y 2019 *Nat. Commun.* **10** 2326
[36] Sun S, He Q, Hao J, Xiao S, and Zhou L 2019 *Adv. Opt. Photonics* **11** 380
[37] Sun Y, Wang C, Yuan H, Sun W, Yuan X, Jin M, Wang Q, and Chen M 2023 *Adv. Opt. Mater.* **11** 2300318
[38] Xu S, Dong F Y, Guo W R, Han D D, Qian C, Gao F, Su W M, Chen H, and Sun H B 2020 *Sci. Adv.* **6** eabb3755
[39] Cao Y, Fu Y, Gao L, Chen H, and Xu Y 2023 *Phys. Rev. A* **107** 013509
[40] Xu Y, Chan C T, and Chen H 2015 *Sci. Rep.* **8** 681
[41] Cao Y, Fu Y, Zhou Q, Xu Y, Gao L, and Chen H 2019 *Opt. Express* **27** 7857